Hierarchical nitrogen doped bismuth niobate architectures: Controllable synthesis and excellent photocatalytic activity

Jungang Hou*, Rui Cao, Zheng Wang, Shuqiang Jiao*, Hongmin Zhu

School of Metallurgical and Ecological Engineering, University of Science and Technology Beijing, Beijing 100083, China

ABSTRACT

Nitrogen doped bismuth niobate ($N-Bi_3NbO_7$) hierarchical architectures were synthesized via a facile two-step hydrothermal process. XRD patterns revealed that the defect fluorite-type crystal structure of Bi_3NbO_7 remained intact upon nitrogen doping. Electron microscopy showed the $N-Bi_3NbO_7$ architecture has a unique peony-like spherical superstructure composed of numerous nanosheets. UV–vis spectra indicated that nitrogen doping in the compound results in a red-shift of the absorption edge from 450 nm to 470 nm. XPS indicated that [Bi/Nb]—N bonds were formed by inducing nitrogen to replace a small amount of oxygen in $Bi_3NbO_{7-x}N_x$, which is explained by electronic structure calculations including energy band and density of states. Based on observations of architectures formation, a possible growth mechanism was proposed to explain the transformation of polyhedral-like nanoparticles to peony-like microflowers via an Ostwald riping mechanism followed by self-assembly. The $N-Bi_3NbO_7$ architectures due to the large specific surface area and nitrogen doping exhibited higher photocatalytic activities in the decomposition of organic pollutant under visible-light irradiation than Bi_3NbO_7 nanoparticles. Furthermore, an enhanced photocatalytic performance was also observed for $Ag/N-Bi_3NbO_7$ architectures, which can be attributed to the synergetic effects between noble metal and semiconductor component.

1. Introduction

Heterogeneous photocatalyst is a research topic of great importance in view of its applications in energy production, global environmental pollutant control, and final chemical synthesis. Many oxide semiconductors, such as TiO_2, ZnO, WO_3, Nb_2O_5 and Bi_2O_3, have been employed as photocatalysts in pollutant degradation and water splitting reactions [1–5]. To date, TiO_2, as a semiconductor photocatalyst with large band gap (about 3.2 eV), has been intensively investigated under UV irradiation ($\lambda < 388$ nm). However, titania can only absorb about less than 5% of sunlight, which greatly limits its practical application [6]. Therefore, the development of visible-light active photocatalysts has become a very important topic of research. Recently, TiO_2 has been modified by transition-metal cations, non-metal anions (such as N, S, C, F) or noble metal nanoparticles for the improvement of the catalytic performance in the visible range [6–10]. For instance, a number of new oxynitride and oxysulphide photocatalysts have been explored through nitrogen doping for environmental and energy applications [11,12]. It indicates that new catalysts with better photocatalytic properties could be developed via homogeneous nitrogen doping route.

Many Bi- or Nb-containing compounds, such as Bi_2WO_6, $BiVO_4$, $BiNbO_4$, Bi_3NbO_7 and $Bi_5Nb_3O_{15}$, are good photocatalysts [13–20]. For instances, Zou and Arakawa reported a series of Bi-doped niobates (i.e., In_2BiNbO_7, Ga_2BiNbO_7, Bi_2InNbO_7, Bi_2GaNbO_7) for water splitting [20]. Ye et al. demonstrated the potential of Bi_2MNbO_7 ($M = Al^{3+}$, Ga^{3+} and In^{3+}), as semiconductor catalysts for phtocatalytic water splitting into H_2 and/or O_2 under UV and visible light irradiation [21]. Lee et al. presented a $PbBi_2Nb_2O_9$ photocatalyst with high activity in the degradation of gaseous isopropyl alcohol and water decomposition [22]. Recently, $BiNbO_4$ and Bi_3NbO_7 as photocatalysts have been also studied for pollutant degradation and water splitting [17–19]. Therefore, it is still a challenge for the development of nitrogen doped bismuth niobate as novel visible-light photocatalyst.

Most of these photocatalysts, with small specific surface area, large particle size, and low adsorbability, are mainly synthesized by the solid-state method at high temperature and only have low photocatalytic activity under the UV light region. All of these undesirable characteristics limit their general applications. In contrast, wet chemical route is a promising alternative, since they can well control the whole process from the molecular precursor to the final material to give highly pure and homogeneous materials. Especially, solution-phase chemical approaches have also been explored for the synthesis of various photocatalysts [23–25]. However, to the best of our knowledge, the synthesis of nitrogen doped Bi_3NbO_7 complex architecture as visible-light photocatalyst has

---

* Corresponding authors. Tel.: +86 10 62334775.
    E-mail addresses: lorinhjg@yahoo.com.cn (J. Hou), sjiao@ustb.edu.cn (S. Jiao).

never been reported via a facile hydrothermal method at lower temperature.

In this work, the influences of synthesis parameters on the resulting products, the synthesis mechanism, the critical roles of treatment conditions and catalyst compositions in determining catalytic performance, as well as the contribution of the work to the fields of visible-light photocatalytic activities were elaborated in detail. There are several significant aspects of the work described in this paper. Firstly, the synthesis of shape-controlled and three dimensional (3D) N-Bi_3NbO_7 architectures have been found to be extremely evasive to date. Hence, a facile two-step hydrothermal synthesis of N-Bi_3NbO_7 architectures with well controlled shape and sizes should be an important progress that may inspire subsequent catalytic materials synthesis. Secondly, catalysis by Bi_3NbO_7 nanoparticles has been studied recently [17,18], but the development of the 3D N-Bi_3NbO_7 architectures and the heterostructured metallic silver-layered bismuth niobate two-component system associated optical properties and photocatalytic activities in the degradation of methylene blue (MB) under visible-light irradiation has been rarely reported. Hence, this work may be of interest to both materials scientists and those working in the area of catalyst design.

2. Experimental

2.1. Synthesis of N-Bi_3NbO_7 architectures

All chemicals were analytical grade and used without further purification. In this work, N-Bi_3NbO_7 architectures were synthesized by a two-step hydrothermal process. The first step was carried out to fabricate niobic acid ($Nb_2O_5 \cdot nH_2O$) by a facile hydrothermal route. In a typical procedure, about 1 g of Nb_2O_5 powder was added to 20 mL of 2 mol L^{-1} KOH solution and desired amounts of $NH_3 \cdot H_2O$, which was loaded into a 30 mL Teflon-lined cylindrical autoclave. Then the sealed autoclave was heated at 200 °C for 4 h, a clear solution was obtained. The pH of the solution was slowly and accurately adjusted to 5.5 by drop-wise adding HCl solution and the precipitated niobic acid was filtered and washed to eliminate all potassium ions. Freshly precipitated niobic acid was added into an aqueous solution of oxalic acid. The solution was stirred at 80 °C until all niobic acid was dissolved. A white milky suspension was then obtained when stochiometric amounts of $Bi(NO_3)_3 \cdot 5H_2O$ and urea with different contents were added in the above solution. The molar ratio of niobium and bismuth was 1:3. The pH value of the suspension was adjusted to 12 by adding drop-wise a concentrated aqueous solution of KOH (3 mol L^{-1}). The suspension was immediately transferred into a 30 mL Teflon-lined stainless steel autoclave up to 80% of the total volume. The autoclave was heated at 140 °C for 12 h. The system was then cooled to ambient temperature naturally, and the products were deposited at the bottom of the vessel. After hydrothermal processing, the resultant samples were collected by centrifugation and washed with deionized water. Finally, the samples were dried at 80 °C for characterization and photocatalytic reaction. Besides, the Bi_3NbO_7 nanoparticles were also prepared via the two-step hydrothermal process and the sol–gel method without the use of urea for comparison (the details were shown in supporting information). Samples were noted as U0, U0.1, U0.2, U0.3, U0.4, U0.5 and U1.5, respectively, according to the content of urea, 0–1.5 g.

In addition, Ag/N-Bi_3NbO_7 heterostructures were suspended in $AgNO_3$ solution (0.1 mg mL^{-1}). The resulting suspension was illuminated by a 300 W Xe lamp for 1 h under magnetic stirring. During illumination, the suspension was recovered by centrifugation and then rinsed continuously with distilled water until no Ag

was detected in the eluate. Finally, the product was dried in an oven at 40 °C for 12 h.

2.2. Calculations

The optimized Bi_3NbO_7 and N-Bi_3NbO_7 model was calculated and the ground-state energy band by using the standard CASTEP package. The CASTEP code is a plane-wave pseudopotential total energy calculation method that is based on the density functional theory (DFT). In our calculational study, the electronic wave functions were expanded in a plane-wave basis set up to a 340 eV cutoff. And the self-consistent field (SCF) tolerance was 1×10^{-6} eV/atom. The ultrasoft pseudopotential and $3 \times 3 \times 3$ k-point for samples were chosen in the calculation. The electronic exchange-correlation energy was treated within the framework of the generalized gradient approximation (GGA), which was superior to the local density approximation (LDA). The calculations of the energy band and density of states (DOS) were both executed.

2.3. Characterization

The obtained products were characterized with X-ray diffraction (XRD) in the range 10–90° using an X-ray diffractometer (Cu K$_\alpha$ radiation, λ = 1.54178 Å). Transmission electron microscopy operated at an accelerating voltage of 200 kV. The high resolution TEM image was acquired using a JEOL 4000EX microscopy, operated at 400 kV. The chemical states of the samples were determined by X-ray photoelectron spectroscopy (XPS) in a VG Multilab 2009 system (UK) with a monochromatic Al K$_\alpha$ source and charge neutralizer. The binding energies were charge corrected using adventitious carbon as a reference. The surface states of the photocatalysts before and after degradation reaction. The surface area of the samples was measured by TriStar 3000-BET/BJH surface area. The UV–vis absorbance spectra were obtained for the samples using a scan UV–vis spectrometer (Shimadzu UV-2550, Japan).

2.4. Photocatalytic test

Photocatalysis reactions were performed in an air-free, closed gas circulation system with a quartz reaction cell. Photocatalytic activity was evaluated by the degradation of methylene blue in aqueous solution under visible-light irradiation using a 300 W Xe lamp with a cutoff filter (λ > 420 nm). A cylindrical Pyrex flask (200 mL) was placed in a sealed black box of which the top was open and the cutoff filter was set on the window face of the reaction vessel to ensure the desired irradiation condition. In each experiments, the samples as catalysts (0.2 g) were added into methylene blue solution (1×10^{-4} M, 100 mL). Before illumination, the suspension between photocatalyst powders and methylene blue at given time intervals (3 mL aliquots) were sampled and centrifuged to remove photocatalyst powders. The filtrates were analyzed by recording the variations of the absorption-band maximum (655 nm) in the UV–vis spectrum of methylene blue in aqueous solution using a UV–vis spectrophotometer (Shimadzu 2550, Japan).

3. Result and discussion

3.1. Characterization of N-Bi_3NbO_7 architectures

The phase composition and crystallinity of the as-prepared N-Bi_3NbO_7 architectures were characterized by XRD, as shown in Fig. 1. Predominantly characteristic peaks can be indexed according to Bi_3NbO_7 crystalline phase (JCPDS, Card No. 86-0875), which is in agreement with the previous works [17]. It illustrates that doping with nitrogen does not result in the development of new crystal orientations or changes in preferential orientations. These
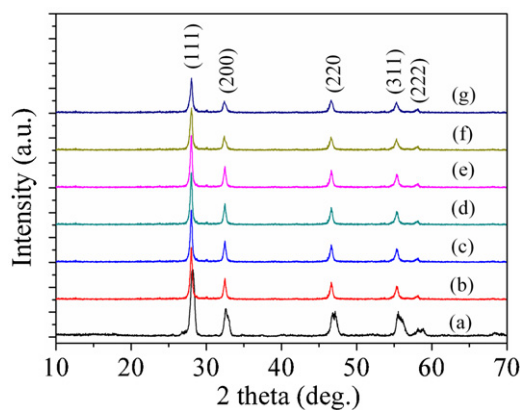
Fig. 1. XRD patterns of as-prepared N-Bi$_3$NbO$_7$ samples using urea with different contents: (a) 0 g; (b) 0.1 g; (c) 0.2 g; (d) 0.3 g; (e) 0.4 g; (f) 0.5 g; and (g) 1.5 g.

peaks in the patterns were indexed to $(1\,1\,1)$, $(2\,0\,0)$, $(2\,2\,0)$, $(3\,1\,1)$ and $(2\,2\,2)$ planes, respectively, which indicates that all samples are constituted of pure cubic Bi$_3$NbO$_7$ phase, in despite of the presence of dopant. However, a careful comparison of the $(1\,1\,1)$ diffraction peaks in the range of $2\theta = 27.5$–$29°$ shows that the peak position of Bi$_3$NbO$_7$ with various nitrogen contents shifts slightly toward a lower 2θ value. Upon appropriate N-doping, the resultant Bi$_3$NbO$_{7-x}$N$_x$ retained the defect fluorite-type crystal structure of Bi$_3$NbO$_7$, while the lattice parameters changed very slightly, i.e., $a = b = c = 5.4793$ Å. This change was possibly due to the incorporation of the N atom into the hexahedral MO$_7$ (M = Bi^{3+} and Nb^{5+}). Ji et al. and Wang et al. have been suggested that the extent of N-doping is very important for optimizing photocatalytic performance [26,27]. Thus, it is vital to the functionality of the photocatalyst, retaining the original crystal structure.

The morphology and microstructure of the as-prepared samples was revealed by SEM and TEM techniques. The morphology of the as-synthesized samples using the different contents of urea was investigated by SEM. For U0.1 sample, the nanoparticles were obtained in Fig. 2a. For U0.2 and U0.3 samples, a large number of nanoparticles with parts of nanosheets were observed in Fig. 2b and c. Fig. 2d shows the SEM image of the product at a higher magnification and indicated the single N-Bi$_3$NbO$_7$ architecture had a unique peony-like spherical superstructure. Besides, the SEM image with low magnification was shown in Fig. S1. It was observed that the microsphere was composed of numerous nanosheets, as shown in Fig. 2b, and macropores or mesopores may be formed among these nanosheets. It revealed that the product was composed of a large quantity of microspheres with an average diameter of about 3 μm. Furthermore, the architectures were decomposed for U0.5 sample and many nanosheets were produced for U1.5 sample. Thus, the content of urea plays a key role in the formation of these architectures.

Based on the above observations, the growth mechanism of the architectures shown in Fig. S2 is proposed. In the initial stage of hydrothermal treatment for 3 h, parts of nanosheets and numerous nanoparticles with a relatively small particle size appear through aggregation (Fig. S2). After 12 h at 140 °C, 3D peony-like N-Bi$_3$NbO$_7$ architectures were obtained via an Ostwald riping mechanism followed by self-assembly (Fig. S2). With increasing time of hydrothermal treatment up to 24 h, the microflowers broke up and transformed into a large number of nanosheets (Fig. S2). Besides, the flow-chart of this two-step hydrothermal process shown in Fig. S2 is proposed. In conclusion, the contents of urea and the hydrothermal treatment time play a pivotal role in controlling the evolution of the complex architectures.

Further investigation was carried out by TEM to reveal the structure of such complex architectures. Fig. 3a shows typical TEM image of polyhedral-like Bi$_3$NbO$_7$ nanoparticles prepared by the two-step hydrothermal process without the use of urea. Involving in the use of 0.4 g urea, TEM image of N-Bi$_3$NbO$_7$ hierarchical architecture was shown in Fig. 3b. Obviously, more unequal nanosheets assembled into fringes of microsphere can be seen. The HRTEM image shown in Fig. 3c was investigated on the fringe part of a thin plate area. The lattice interplanar spacing was measured to be 0.324 nm, which was different with the previous work due to the incorporation of the N atom because the d values shift proportionally to the amount of doped nitrogen according to the Vegard's law [17,28]. The selected-area electron diffraction (SAED) pattern of this part was shown in Fig. 3d. The pattern exhibited a clear cubic diffraction spot array and could be indexed to the single crystalline Bi$_3$NbO$_7$.

Full nitrogen sorption isotherms of the 3D hierarchical N-Bi$_3$NbO$_7$ architecture were measured to gain the information about the specific surface area, as shown in Fig. 4. The specific surface area was calculated to be 103 m^2 g^{-1} by the BET equation, as shown in Fig. 4b. The corresponding Barrett Joyner Halenda (BJH) analyses (the inset in Fig. 4) exhibit that most of the pores fall into the size range from 10 to 80 nm. These pores presumably arise from the spaces among these nanosheets within hierarchical N-Bi3NbO7 architectures. Although the relatively low surface area for Bi$_3$NbO$_7$ nanoparticles results from its high density, the present surface area data of the flower-like N-Bi$_3$NbO$_7$ architectures is much higher than that of the polyhedral-like Bi$_3$NbO$_7$ nanoparticles (the specific surface area was calculated to be 13 m^2 g^{-1}, as shown in Fig. 4a). The high surface area and mesoporous structure of the hierarchical N-Bi$_3$NbO$_7$ structures provide the possibility for the efficient diffusion and transportation of the degradable organic molecules and hydroxyl radicals in photochemical reaction, which will lead to the enhanced photocatalytic performance of N-Bi$_3$NbO$_7$ materials.

The relationship of nitrogen and metal oxides through the ammoniate treatment as the nitrogen source has been paid more attention in the literatures [29]. However, the introduction of nitrogen through this hydrothermal process has been rarely reported. In order to reveal the very essential part of the nitrogen-doped Bi$_3$NbO$_7$, the chemical states of as-prepared Bi$_3$NbO$_7$ architectures shown in Figs. 5 and 6 were carefully checked by the X-ray photoelectron spectroscopy (XPS), containing Bi, Nb, O and N.

The Bi 4f fine XPS spectra of the N-Bi$_3$NbO$_7$ sample is presented in Fig. 5b. XPS signals of Bi 4f were observed at binding energies at around 164.2 eV (Bi 4f$_{5/2}$) and 158.8 eV (Bi 4f$_{7/2}$) ascribed to Bi^{3+}, which are consistent with the data of Bi$_2$O$_3$ powders [30]. The Nb 3d fine XPS spectra of the N-Bi$_3$NbO$_7$ sample is shown in Fig. 5c. XPS signals of Nb 3d were observed at binding energies at around 210.18 eV (Nb 3d$_{5/2}$) and 212.88 eV (Nb 3d$_{3/2}$). The Nb 3d peaks were in good agreement with the previous work [17]. In Fig. 5d, it can be seen that the O 1s peak is fitted into the peak centering at 529.6 eV, which is mainly assigned to the oxygen in the prepared sample lattice [30].

The N 1s fine XPS spectra of the N-Bi$_3$NbO$_7$ samples were shown in Fig. 6. A shoulder at around 399.6 eV was observed for the N-Bi$_3$NbO$_7$ samples using urea with different contents. The peak at around 399.6 eV was assigned to N 1s. The Nb 3d and N 1s curve fitting XPS spectra of the N-Bi$_3$NbO$_7$ samples were also shown in Fig. S3. The previous work reported by Ye's group also demonstrated that nitrogen can be doped into the sample using urea in the similar preparation [31].

3.2. Calculation of the density of states

The electronic structures of the Bi$_3$NbO$_7$ and N-Bi$_3$NbO$_7$ were calculated by the plane-wave-density function theory (DFT) using CASTEP program package. Fig. 7ab and cd plot the calculated
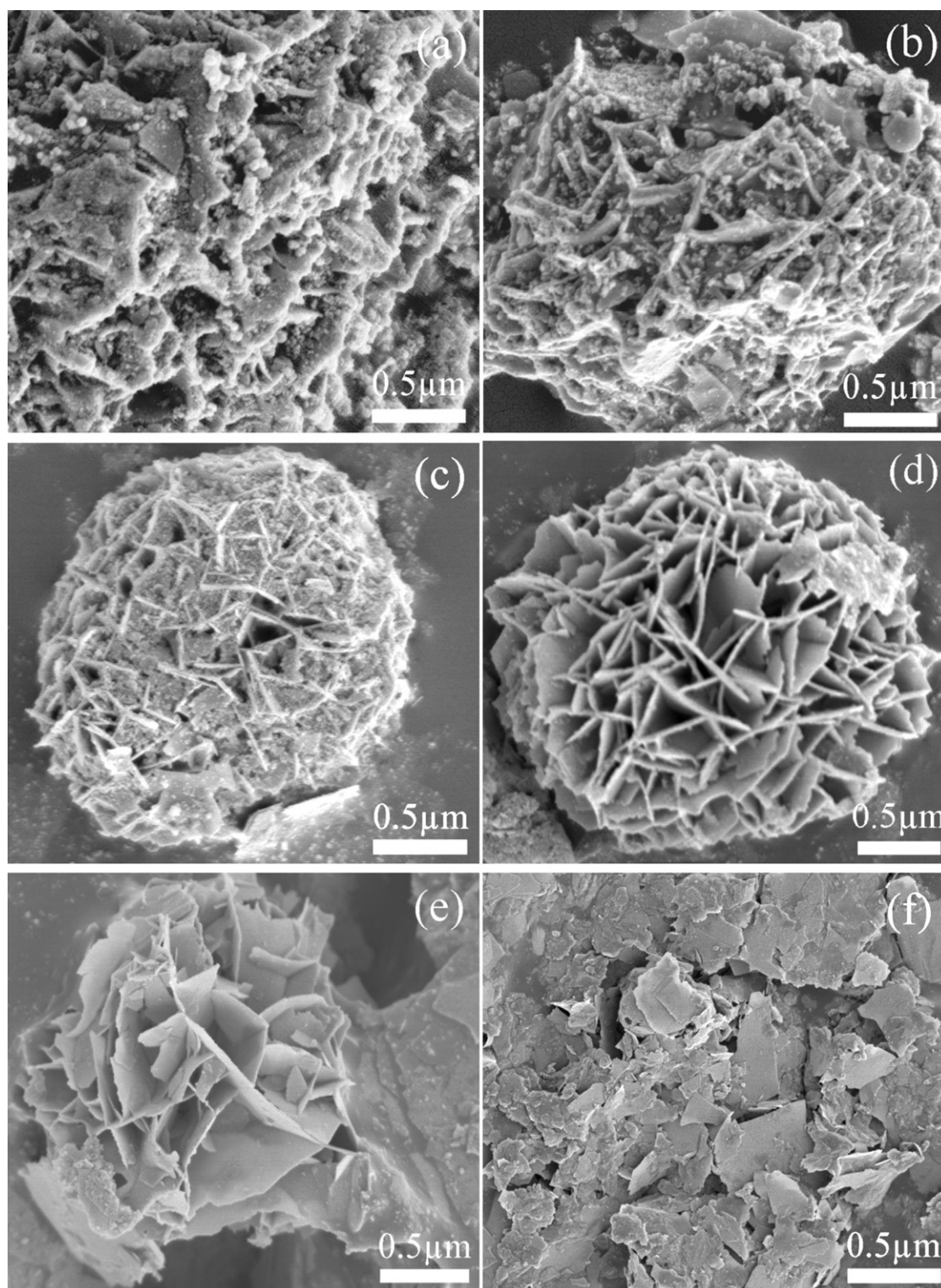
Fig. 2. SEM images of as-prepared N-Bi$_3$NbO$_7$ architectures using urea with the various contents: (a) 0.1 g; (b). 0.2 g; (c) 0.3 g; (d) 0.4 g; (e) 0.5 g; (f) 1.5 g.

energy band and total density of states (TDOS) for the Bi$_3$NbO$_7$ and N-Bi$_3$NbO$_7$ containing oxygen vacancy, respectively. Besides, the projected density of states (PDOS) of Bi$_3$NbO$_7$ and N-Bi$_3$NbO$_7$ are shown (see Figs. S4 and S5). The calculated band gaps of the Bi$_3$NbO$_7$ and N-Bi$_3$NbO$_7$ were 2.64 eV and 2.47 eV, respectively, which is a little smaller than that of the experimental band gap. The difference mainly results from the well-known shorting

coming of exchange-correction function in describing excited states in the DFT calculation.

To explore the details of the electronic properties, it can be seen that there is no spin polarization for all models from TDOS and PDOS. For the Bi$_3$NbO$_7$ and N-Bi$_3$NbO$_7$ structures, Bi 6s states contribute mainly to the valance band and Bi 6p states to the conduction band. For the Bi$_3$NbO$_7$ (Fig. 7ab), it is clear that the valence
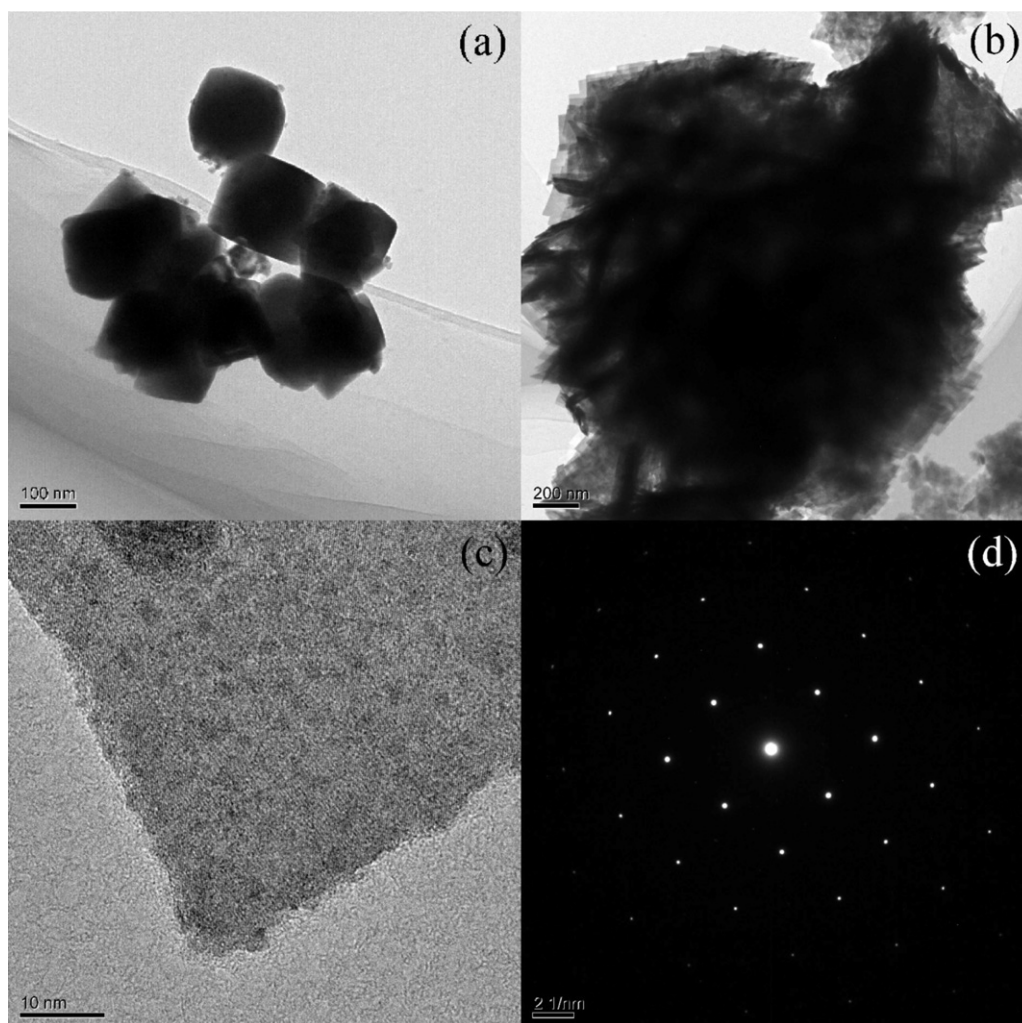
Fig. 3. TEM images of as-prepared N–Bi$_3$NbO$_7$ samples without (a) or with (b) urea. HRTEM image (c) and selected electron diffraction pattern (d) of N–Bi$_3$NbO$_7$ nanosheet.

band top mainly consists of O 2p and Bi 6s orbitals. The conduction band bottom is mainly constructed of the Bi 6p, O 2p and Nb 4d orbitals.

For a further investigation, the TDOS and PDOS of N 2p states are shown (Fig. 7 and Fig. S7), it can be seen that the N 2p states mainly contribute to the formation of impurity energy levels hybridized by O 2p states and Bi 6s states as the valence band of

the doped Bi$_3$NbO$_7$ structures, accompanied by the presence of the oxygen vacancies. In particular, Bi$_3$NbO$_7$ has a network structure constructed of three-dimensional edge-sharing hexahedral MO$_7$ (M = Bi^{3+} and Nb^{5+}). In each hexahedral MO$_7$ (M = Bi^{3+} and Nb^{5+}), the metallic atom is surrounded by seven oxygen atoms placed at the apex of a cube, leaving one of the positions vacant [18]. The nitrogen doping occurs due to the substitution of oxygen by nitrogen anions in the hexahedron. For the interstitial nitrogen-doped Bi$_3$NbO$_7$, the isolated impurity level is located above the valence band maximum (VBM). In addition, an add-on shoulder is present on the edge of the VBM. Thus, gap levels consisting of N 2p states are introduced within the band gap of the Bi$_3$NbO$_7$ structures leading to band gap narrowing, which may result in the enhancement of photocatalytic absorption and activity under visible-light irradiation.

3.3. Measurement of the light absorption

The optical absorption of the Bi$_3$NbO$_7$ and N–Bi$_3$NbO$_7$ samples was measured by UV–vis diffuse reflection spectroscopy, and the results are shown in Fig. 8. For the N–Bi$_3$NbO$_7$ samples, the absorbance intensity in the wave length range from 450 to 470 nm increased as the content of urea increased. The calculated band gaps of the U0 and U0.4 samples were 2.75 eV and 2.61 eV, respectively. Utilizing visible light for driving photocatalytic reactions is a key challenge and visible light absorption of a material is a prerequisite
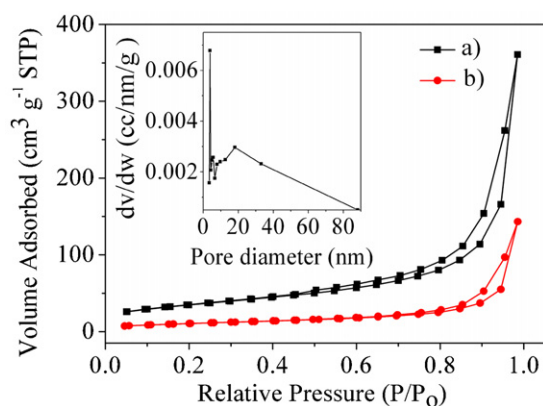

Fig. 4. Typical N$_2$ gas adsorption desorption isotherms of the 3D hierarchical N–Bi$_3$NbO$_7$ architecture (a) and Bi$_3$NbO$_7$ nanoparticles (b). The inset is the corresponding pore-size distribution.
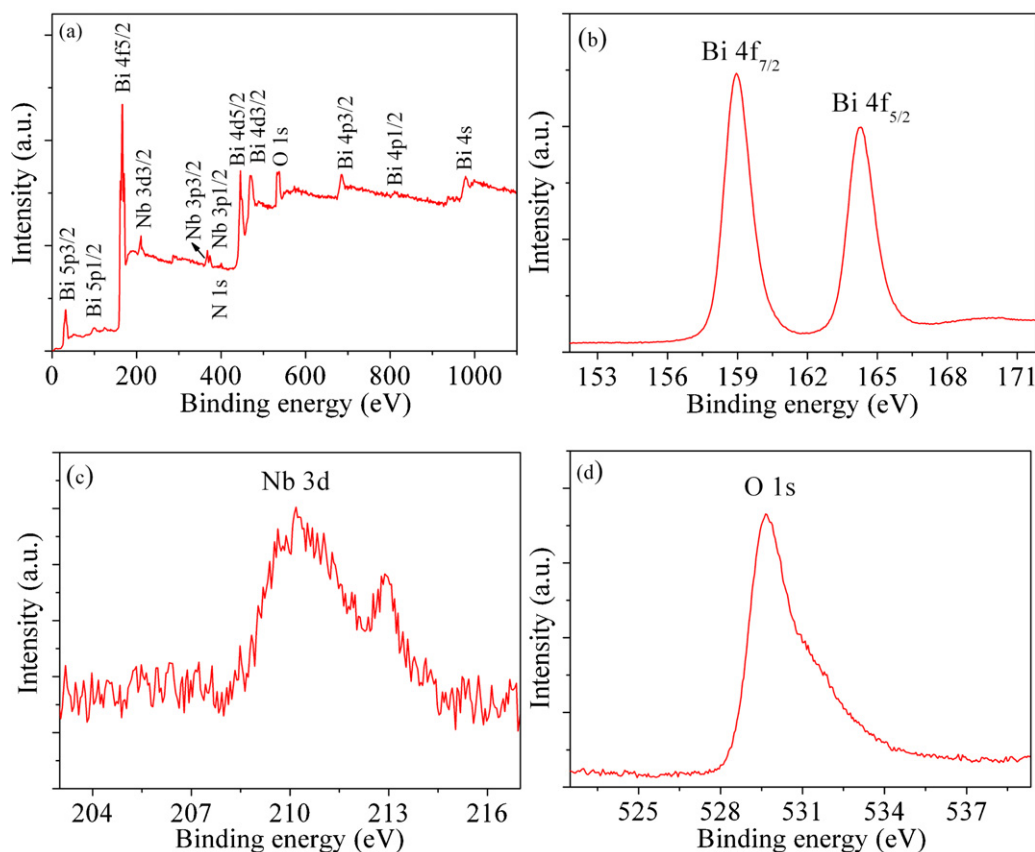
Fig. 5. XPS spectra of (a) survey spectrum, (b) Bi 4f, (c) Nb 3d, and (d) O 1 s for the N–Bi$_3$NbO$_7$ architectures.

for visible light activity. The extension of the light absorption within the visible range arises from the contributions of the doped nitrogen atoms, because the interstitial nitrogen atoms induced the local states near the valence band edge [29].

3.4. Evaluation of photocatalytic activities

The photocatalytic activities of the samples were evaluated by monitoring the decomposition of MB in an aqueous
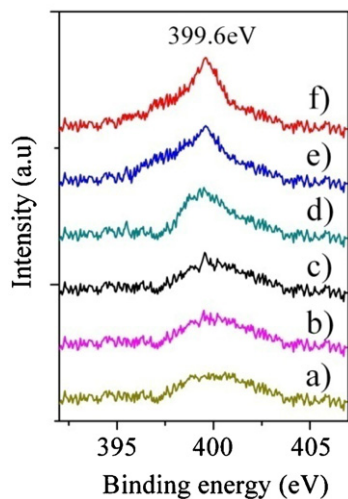
Fig. 6. High resolution XPS spectra of the N 1s core level obtained from the N-Bi$_3$NbO$_7$ samples using urea with different contents: (a) 0.1 g; (b) 0.2 g; (c) 0.3 g; (d) 0.4 g; (e) 0.5 g; and (f) 1.5 g.

solution under visible light irradiation, respectively. MB solution is also a common model pollutant to test the photodegradation capability of the N-Bi$_3$NbO$_7$ samples. Fig. 9a shown the degradation curve of methylene blue catalyzed by the Bi$_3$NbO$_7$ and N-doped Bi$_3$NbO$_7$ under visible light irradiation. A trend in the photocatalytic activity has been observed in the following order: U0.4 > U0.5 > U0.3 > U1.5 > U0.2 > U0.1 > U0. The photocatalytic activity of the N-doped Bi$_3$NbO$_7$ architectures upon visible light irradiation increased with the N content except for sample U1.5 (as shown in Fig. S6). Almost complete degradation of MB (the degradation efficiency, $R\%$ is about 99%) for the N-doped Bi$_3$NbO$_7$ architectures (U0.4) was achieved when exposed to visible light irradiation for 120 min while the $R\%$ is only about 37% with the use of the Bi$_3$NbO$_7$ nanoparticles. Currently, the photocatalytic activity of Bi$_3$NbO$_7$ nanoparticles prepared by this two-step hydrothermal process is higher than that of the sol–gel method (as shown in Fig. S7). Among these samples, U0.4 samples exhibited a gradually enhanced photoactivity for MB degradation as compared to U0–U1.5 samples. The color of the suspension changed light gradually and disappeared ultimately, as shown in Fig. 9b. Currently, the direct decomposition of MB without the presence of photocatalysts was almost negligible under visible light irradiation in a control experiment (as shown in Fig. 10).

The high visible-light photocatalytic activity of the N-doped Bi$_3$NbO$_7$ architectures may result from the several reasons. More importantly, the urea existing in synthesis of the N-doped Bi$_3$NbO$_7$ nanostructures has effects on the BET surface area of the photocatalyst, which is in agreement with the analysis from Fig. 4. Besides, the introduction of nitrogen in Bi$_3$NbO$_7$ architectures promotes the separation of photogenerated charges. This may lead to the formation of new active sites, which are responsible for the observed higher photocatalytic activity. It is known that the positions of the
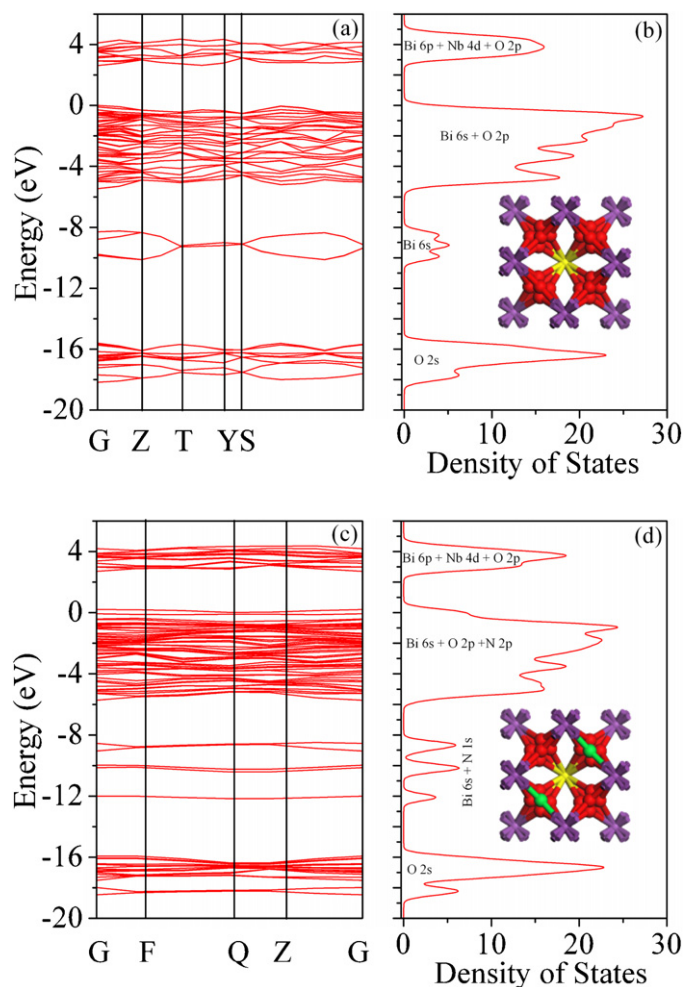
Fig. 7. The calculated energy band and density of states (DOS) of pure phase of Bi_3NbO_7 (a and b) and nitrogen doped Bi_3NbO_7 (c and d). Inset of the crystal structure of Bi_3NbO_7 and $N-Bi_3NbO_7$ by the ball-and-stick mode (purple: bismuth; yellow: niobium; red: oxygen; and green: nitrogen). (For interpretation of the references to color in this figure legend, the reader is referred to the web version of the article.)

valence band maximum (VBM) and the conduction band minimum (CBM) are critical variables in determining the feasibility of efficient degradation. As exemplified earlier in the calculations, the increase in the VBM without altering the CBM as a result of N-doping reduces the overall band-gap and thus forms intermediate steps higher than
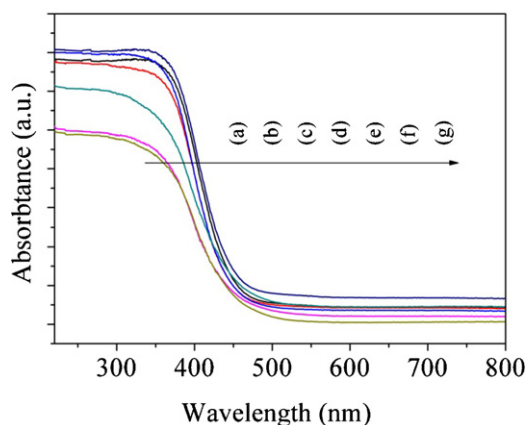

Fig. 9. Evaluation of photocatalytic activities (a) and UV–visible spectra changes in MB degradation with U0.4 samples (b) under visible-light irradiation.

the VBM formed as a result of N 2p and O 2p orbital mixing, resulting in the generation of •OH radicals and thus causing greater solar light absorption in the visible light region without having any effect on the CBM. Based on the above experimental results, we have demonstrated that an optimized amount of urea is essential to enhance the photoactivity. The N-doped Bi_3NbO_7 architectures exhibit the highest photocatalytic ability due to the synergic effect of the obvious improvement in the nanostructure surface area and absorption of the dye, and the fast transfer rate of photogenerated electrons from N-doped Bi_3NbO_7 architectures to organic pollution through nitrogen. Therefore, it is proposed that the appropriate amount of

Fig. 8. UV–vis diffuse reflectance spectra of the $N-Bi_3NbO_7$ samples using urea with different contents: (a) 0 g; (b) 0.1 g; (c) 0.2 g; (d) 0.3 g; (e) 0.4 g; (f) 0.5 g; and (g) 1.5 g.
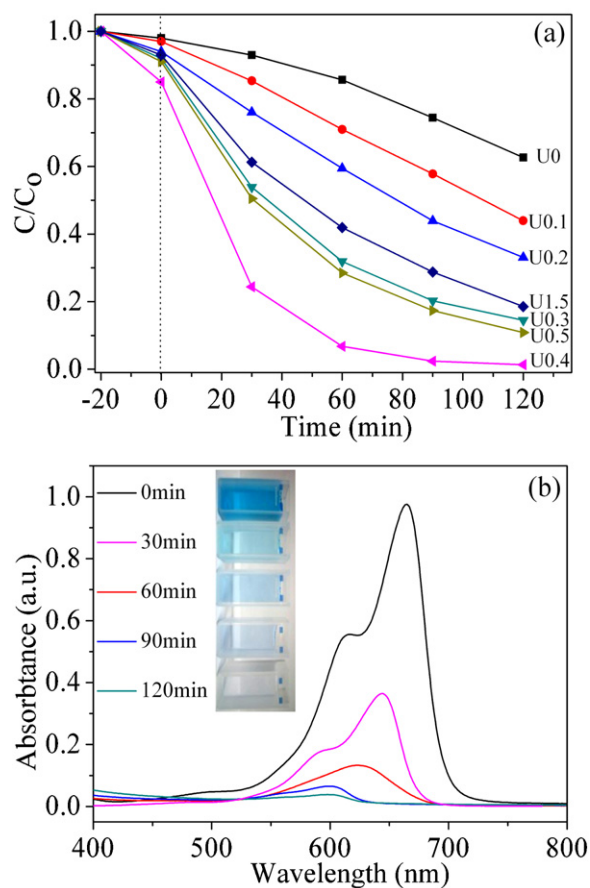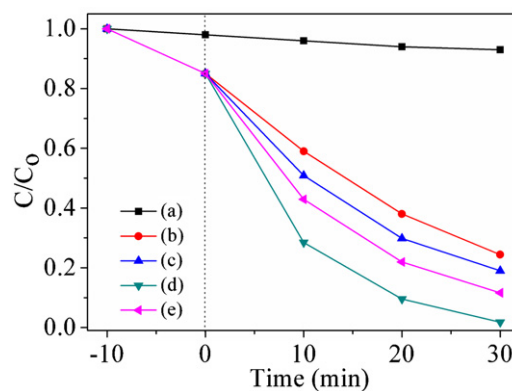

Fig. 10. Photodegradation efficiencies of MB as a function of visible-light irradiation time by different photocatalysts: (a) MB; (b) U0.4; (c) 1%Ag/U0.4; (d) 5%Ag/U0.4; and (e) 10%Ag/U0.4.
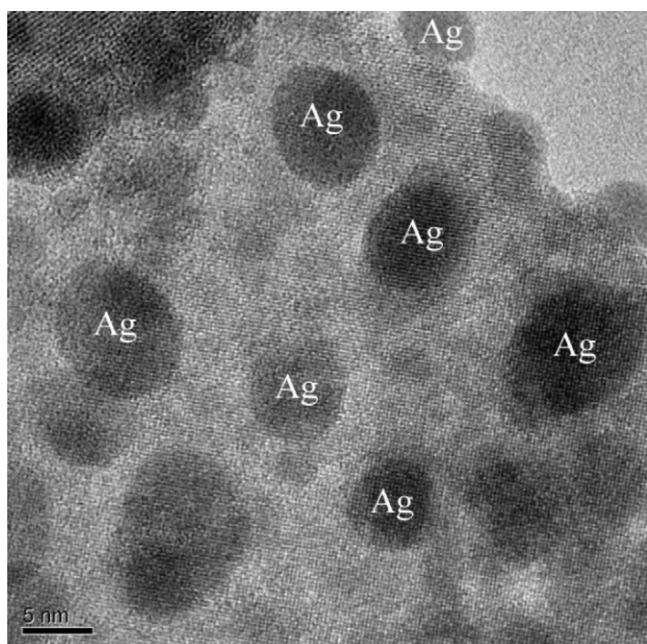
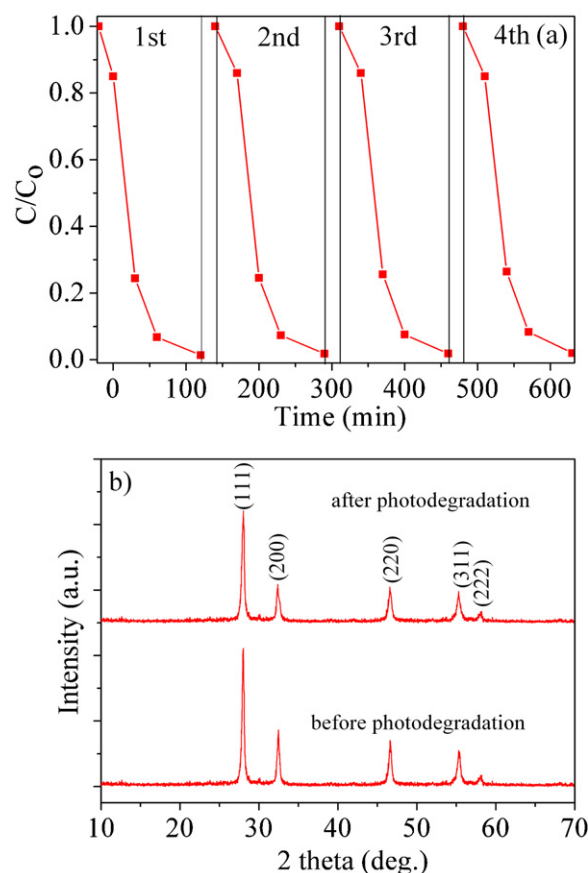Fig. 11. TEM image of U0.4 samples decorated with 5 wt.% Ag nanoclusters.

Fig. 12. Cycling runs in MB degradation with U0.4 as photocatalysts under visible-light irradiation (a); XRD patterns of U0.4 samples before and after photodegradation.

urea can significantly facilitate the separation of photogenerated electron–holes and enhance the photocatalytic degradation efficiency. However, the excess urea in the hydrothermal process will result into deformation of 3D architectures and excessive nitrogen, which can prevent the inherent optical absorption of Bi_3NbO_7 samples and result in the rapid decrease of the quantity of photogenerated charges, and finally reduce the photoactivity. More detailed researches are desired to understand the high visible-light activity of N-doped Bi_3NbO_7 architectures. The investigation on more detailed structure of the N-doped Bi_3NbO_7 architectures is in progress to clarify the improvement of visible-light photocatalytic activity.

Recently, semiconductor-based heterostructure crystals have attracted much research attention. On the basis of the previous study about the promising application of metal/oxides nanocrystals [19], an enhanced photocatalytic performance for its degradation shown in Fig. 10 was also observed for the heterostructured metallic silver-layered bismuth niobate two-component system. Especially, the relationship between their contents and photocatalytic activities was also investigated in this work. It can see that the Ag/N-Bi_3NbO_7 heterostructure catalysts with an Ag content of 5% show the highest photocatalytic activity. The SEM image of the Ag nanoclusters decorated on N-Bi_3NbO_7 nanosheets were shown in Fig. 11, demonstrating the size of Ag particles is about 2–6 nm. When an Ag content is relatively lower (5%), the photocatalytic activity of the Ag/N-Bi_3NbO_7 heterostructure increases gradually with an increase of the Ag content (5%Ag/U0.4 > 1%Ag/U0.4 > U0.4). However, when the Ag content exceeds 5%, the photocatalytic activity of the Ag/N-Bi_3NbO_7 heterostructure decreased with an increase of the Ag content (5%Ag/U0.4 > 10%Ag/U0.4).

It is worth pointing out that the stability of a given photocatalyst during photoreaction is a crucial factor for the practical applications. The stability tests were investigated by carrying out recycling reactions four times for the photodegradation of MB over the N-Bi_3NbO_7 samples under visible light irradiation and the results are shown in Fig. 12. No decrease in catalytic activity was observed in the recycling reactions. Combined with the XRD patterns, all evidences demonstrate that the N-Bi_3NbO_7 has good stability. In addition, the catalytic stability of the Ag/N-Bi_3NbO_7 heterostructure catalyst with a Ag content of 5% is carried out (as shown in

Fig. S8). It shows that this catalyst has an excellent catalytic stability because of the high crystallinity of the synthesized sample.

In order to have an in-depth understanding of the catalytic mechanism, the schematic diagram of photocatalytic mechanism for Ag/N-Bi_3NbO_7 samples was shown in Fig. 13. The deposition of noble metals on semiconductor nanoparticles is an effective way for improving the photocatalytic efficiency as the metal modifier
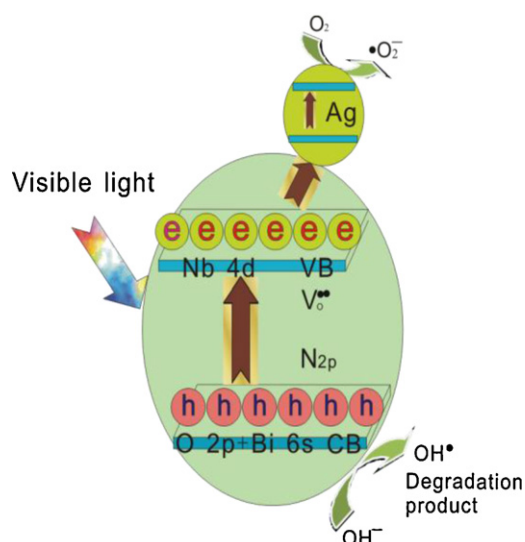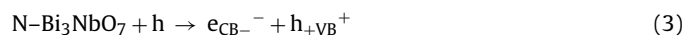

Fig. 13. Schematic diagram of photocatalytic mechanism for Ag/N-Bi_3NbO_7 samples.

can indirectly influence the interfacial charge transfer processes. Certainly, a primary understanding of photoinduced interactions as well as the interfacial charge transfer processes in metal-modified semiconductors is important to explain the exact role of metal in semiconductor photocatalysis. Light absorption of a suitable wavelength by $N-Bi_3NbO_7$ results in the promotion of an electron from the valence band to the conduction band. The resulting hole is primarily responsible for the formation of hydroxyl radicals, which subsequently degrade the pollutants adsorbed onto the surface of the photocatalyst. In the previous work, the overall photocatalytic reaction is ascribed to the molecular oxygen reduction to $\bullet O_2^-$ [32,33]. The photoinduced holes can be easily trapped by OH^- to further produce a hydroxyl radical species ($OH^\bullet$), which is an extremely strong oxidant for the partial or complete mineralization of organic chemicals. Therefore, the photocatalytic reaction process can be proposed as follows:

$$Ag \rightarrow Ag^+ + e^- \tag{1}$$

$$e^- + O_2 \rightarrow \bullet O_2^- \tag{2}$$

$$N-Bi_3NbO_7 + h \rightarrow e_{CB-}^- + h_{+VB}^+ \tag{3}$$

$$e_{CB-}^- + Ag^+ \rightarrow Ag \tag{4}$$

$$h_{+VB}^+ + OH^- \rightarrow OH^\bullet \tag{5}$$

Based on the above-mentioned discussion, it is proposed that Ag nanoparticles on the surface of $N-Bi_3NbO_7$ architecture with $V_o^{\bullet\bullet}$ defect act as a sink for the electrons (Eqs. (1) and (4)), improve the separation of photogenerated electron hole pairs, and thus enhance the visible-light-driven photocatalytic activity of $Ag/N-Bi_3NbO_7$ heterostructural architectures as photocatalysts.

4. Conclusion

Nitrogen doped bismuth niobate hierarchical architectures as novel photocatalysts were successfully synthesized via a facile two-step hydrothermal process as a straightforward protocol. The obtained samples were characterized by X-ray diffraction, electron microscopy, X-ray photoelectron spectra, UV–vis diffuse reflectance spectrum and BET surface area. The as-prepared peony-like $N-Bi_3NbO_7$ architectures and polyhedral-like Bi_3NbO_7 nanoparticles own a narrowed band gap of about 2.6–2.75 eV, which is explained by its electronic structure calculations including energy band and density of states, as arising from a Bi-hybridized O 2p-derived valance band and a Bi-hybridized Nb 4d- and O 2p-derived conduction band. Visible light absorption is promoted from the N 2p levels near the valence band maximum. Based on observations of the factors that influence architectures formation, a possible growth mechanism is proposed to explain the transformation of nanoparticles to microflowers via an Ostwald riping mechanism followed by self-assembly. The 3D $N-Bi_3NbO_7$ architectures due to the large specific surface area and nitrogen doping exhibited higher photocatalytic activities in the decomposition of MB solution under visible-light irradiation than Bi_3NbO_7 nanoparticles. Furthermore, an enhanced photocatalytic performance for its degradation was also observed for the heterostructured metallic silver-layered bismuth niobate two-component system, which can be attributed to the synergetic effects between noble metal and semiconductor component. This finding is of significant importance not only because a highly active visible-light photocatalyst is developed using a simple doping route but also it advances the fundamental understanding of the substantial role of uniform nitrogen doping in niobate photocatalyst. Hence, this work is also applicable to the development of uniform anion doping in other niobate or tantalate semiconductors with controllable morphology for applications in solar energy conversion, gas sensors and photoluminescence.

Appendix A. Supplementary data

Supplementary data associated with this article can be found, in the online version, at doi:10.1016/j.jhazmat.2012.03.009.

References

[1] X. Chen, S. Shen, L. Guo, S. Mao, Semiconductor-based photocatalytic hydrogen generation, Chem. Rev. 110 (2010) 6503–6570.
[2] I. Nowak, M. Ziolek, Niobium compounds – preparation, characterization and application in heterogeneous catalysis, Chem. Rev. 99 (1999) 3603–3624.
[3] W.J. Youngblood, S.-H.A. Lee, K. Maeda, T.E. Mallouk, Visible light water splitting using dye-sensitized oxide semiconductors, Acc. Chem. Res. 42 (2009) 1966–1972.
[4] A. Kudo, Y. Miseki, Heterogeneous photocatalyst materials for water splitting, Chem. Soc. Rev. 38 (2009) 253–278.
[5] J. Kim, W. Choi, Hydrogen producing water treatment through solar photocatalysis, Energy Environ. Sci. 3 (2010) 1042–1045.
[6] S. Kim, S. Hwang, W. Choi, Visible light active platinum-ion-doped TiO_2 photocatlyst, J. Phys. Chem. B 109 (2005) 24260–24267.
[7] M. Anpo, M. Takeuchi, The design and development of highly reactive titanium oxide photocatalysts operating under visible light irradiation, J. Catal. 216 (2003) 505–516.
[8] U.M. Shahed, A. Mofareh, B. William, Efficient photochemical water splitting by a chemically modified n-TiO_2, Science 297 (2002) 2243–2245.
[9] S. Sakthivel, H. Kisch, Daylight photocatalysis by carbon-modified titanium dioxide, Angew. Chem. Int. Ed. 42 (2003) 4908–4911.
[10] R. Asahi, T. Morikawa, T. Ohwaki, K. Aoki, Y. Taga, Visible-light photocatalysis in nitrogen-doped titanium oxides, Science 293 (2001) 269–271.
[11] K. Maeda, K. Teramura, D. Lu, T. Takata, N. Saito, Y. Inoue, K. Domen, Photocatalyst releasing hydrogen from water-enhancing catalytic performance holds promise for hydrogen production by water splitting in sunlight, Nature 440 (2006) 295–296.
[12] A. Ishikawa, T. Takata, J.N. Kondo, M. Hara, H. Kobayashi, K. Domen, Oxysulfide $Sm_2Ti_2S_2O_5$ as a stable photocatalyst for water oxidation and reduction under visible light irradiation ($\lambda < 650$ nm), J. Am. Chem. Soc. 124 (2002) 13547–13553.
[13] L.S. Zhang, W.Z. Wang, Z.L. Zhou, Bi_2WO_6 nano- and microstructures: shape control and associated visible-light-driven photocatalytic activities, Small 3 (2007) 1618–1625.
[14] L. Zhou, W.Z. Wang, S.W. Liu, A sonochemical route to visible-light-driven high-activity $BiVO_4$ photocatalyst, J. Mol. Catal. A: Chem. 252 (2006) 120–124.
[15] B. Muktha, J. Darriet, G. Madras, T.N. Guru Row, Crystal structures and photocatalysis of the triclinic polymorphs of $BiNbO_4$ and $BiTaO_4$, J. Solid State Chem. 179 (2006) 3919–3925.
[16] X. Lin, T. Huang, F. Huang, W. Wang, J. Shi, Photocatalytic activity of a Bi-based oxychloride Bi_4NbO_8Cl, J. Mater. Chem. 17 (2007) 2145–2150.
[17] G.K. Zhang, J.L. Yang, S.M. Zhang, Q. Xiong, B.B. Huang, J.T. Wang, W.Q. Gong, Preparation of nanosized Bi_3NbO_7 and its visible-light photocatalytic property, J. Hazard. Mater. 172 (2009) 986–992.
[18] L. Wang, W.Z. Wang, M. Shang, S.M. Sun, W.Z. Yin, J. Ren, J. Zhou, Visible light responsive bismuth niobate photocatalyst: enhanced contaminant degradation and hydrogen generation, J. Mater. Chem. 20 (2010) 8405–8410.
[19] Y. Guo, L. Chen, F. Ma, S. Zhang, Y. Yang, X. Yuan, Y. Guo, Efficient degradation of tetrabromobisphenol A by heterostructured $Ag/Bi_5Nb_3O_{15}$ material under the simulated sunlight irradiation, J. Hazard. Mater. 189 (2011) 614–618.
[20] Z.G. Zou, H. Arakawa, Direct water splitting into H_2 and O_2 under visible light irradiation with a new series of mixed oxide semiconductor photocatalysts, J. Photochem. Photobiol. A 158 (2003) 145–162.
[21] Z.G. Zou, J.H. Ye, H. Arakawa, Hydrogen production and characterization of $MLaSrNb_2NiO_9$ (M = Na, Cs, H) based photocatalysts, Int. J. Hydrogen Energy 28 (2003) 663–669.
[22] H.G. Kim, D.W. Hwang, J.S. Lee, An undoped, single-phase oxide photocatalyst working under visible light, J. Am. Chem. Soc. 126 (2004) 8912–8913.
[23] J.G. Hou, R. Cao, S.Q. Jiao, H.M. Zhu, R.V. Kumar, $PANI/Bi_{12}TiO_{20}$ complex architectures: controllable synthesis and efficient visible light-driven photocatalytic activities, Appl. Catal. B 104 (2011) 399–406.
[24] J.G. Hou, Y.F. Qu, D. Krsmanovic, C. Ducati, D. Eder, R.V. Kumar, Solution-phase synthesis of single-crystalline $Bi_{12}TiO_{20}$ nanowires with photocatalytic property, Chem. Commun. 26 (2009) 3937–3939.

[25] J.G. Hou, Y.F. Qu, D. Krsmanovic, C. Ducati, D. Eder, R.V. Kumar, Hierarchical synthesis of bismuth titanate complex architectures and their visible-light photocatalytic activities, J. Mater. Chem. 20 (2010) 2418–2423.

[26] M.S. Ji, P.H. Borse, H.G. Kim, D.W. Hwang, J.K. Jang, S.W. Bae, J.S. Lee, Photocatalytic hydrogen production from water–methanol mixtures using N-doped $Sr_2Nb_2O_7$ under visible light irradiation: effects of catalyst structure, Phys. Chem. Chem. Phys. 7 (2005) 1315–1321.

[27] A. Mukherji, R. Marschall, A. Tanksale, C. Sun, S. Smith, G. Lu, L. Wang, N-doped $CsTaWO_6$ as a new photocatalyst for hydrogen production from water splitting under solar irradiation, Adv. Funct. Mater. 21 (2011) 126–132.

[28] A.R. Denton, N.W. Ashcroft, Vegard's law, Phys. Rev. A 43 (1991) 3161–3164.

[29] J. Wang, D. Tafen, J. Lewis, Z. Hong, A. Manivannan, M. Zhi, M. Li, N. Wu, Origin of photocatalytic activity of nitrogen-doped TiO_2 nanobelts, J. Am. Chem. Soc. 131 (2009) 12290–12297.

[30] J.G. Hou, R. Cao, Z. Wang, S.Q. Jiao, H.M. Zhu, Chromium-doped bismuth titanate nanosheets as enhanced visible-light photocatalysts with a high percentage of reactive {1 1 0} facets, J. Mater. Chem. 11 (2011) 7296–7301.

[31] X. Li, N. Kikugawa, J. Ye, A comparison study of rhodamine B photodegradation over nitrogen-doped lamellar niobic acid and titanic acid under visible-light irradiation, Chem. Eur. J. 15 (2009) 3538–3845.

[32] H. Goto, Y. Hanada, T. Ohno, M. Matsumura, Quantitative analysis of superoxide ion and hydrogen peroxide produced from molecular oxygen on photoirradiated TiO_2 particles, J. Catal. 225 (2004) 223–229.

[33] Y.H. Zheng, L.R. Zheng, Y.Y. Zhan, X.Y. Lin, Q. Zheng, K.M. Wei, Ag/ZnO heterostructure nanocrystals: synthesis, characterization, and photocatalysis, Inorg. Chem. 46 (2007) 6980–6986.